Solar Energy Materials & Solar Cells 279 (2025) 113262

Contents lists available at ScienceDirect

Solar Energy Materials and Solar Cells

journal homepage: www.elsevier.com/locate/solmat

# Enhancing efficiency of dense array CPV receivers with controlled DC-DC converters and adaptive microfluidic cooling under non-uniform solar irradiance

Desideri Regany [a,*], Francesc Majós Palau [a], Alicia Crespo [a,b], Jérôme Barrau [a], Montse Vilarrubí [a], Joan Rosell-Urrutia [a]

[a] Sustainable Energy, Machinery and Buildings (SEMB) Research Group, University of Lleida, Pere de Cabrera nº3, 25001, Lleida, Spain
[b] Department of Mechanical Engineering, University Rovira i Virgili, Av. Països Catalans 26, 43007, Tarragona, Spain

ARTICLE INFO

*Keywords:*
Concentrating photovoltaics
Mismatch losses
DC-DC converter
Non-uniform illumination
Self-adaptive microfluidic cooling system

ABSTRACT

Concentrating solar technologies offer substantial potential for optimizing solar energy for heat and power generation, particularly in green hydrogen production. This study investigates the use of commercial high efficiency concentrated photovoltaic (CPV) cells in a central tower concentrating solar system to enhance energy conversion efficiency. By integrating DC-DC converters with self-adaptive microfluidic cooling systems, we address current mismatches and temperature variations that affect CPV performance. The novel receiver design ensures scalability for large-scale implementations by implementing the electrical connections between DC-DC converters and each CPV cell without creating shaded areas. We numerically model and simulate the thermodynamic and electrical characteristics of a dense array CPV receiver, evaluating six illumination profiles. Our results indicate a significant improvement in receiver efficiency compared to the traditional configuration with bypass diodes, demonstrating an increase from 23.4 % to 30.3 % under a central Gaussian illumination profile, and reaching up to 38 % relative efficiency improvement depending on the applied profile. Power transfer losses decrease from 26 % to 10 % when 200 kW/m$^2$ of illumination non-uniformity occurs. The proposed solution enhances reliability and energy conversion efficiency, presenting a viable path forward for large-scale CPV applications.

Nomenclature

| Symbols | | | |
|---|---|---|---|
| I | CPV cell current, A | $P_{in\_DC}$ | Power consumption of the DC-DC converters, W |
| $I_{sc}$ | Short-circuit current, A | $P_{out\_receiver}$ | Total receiver power output, W |
| $I_T$ | Total receiver current, A | $P_{net}$ | Net receiver power, W |
| $I_{ph}$ | Solar-generated current for measurements, A | $P_T$ | Total receiver output power, W |
| $I_s$ | Diode saturation current, A | $k_B$ | Boltzmann constant, J/K |
| $I_{r0}$ | Irradiance used for measurements, W/m$^2$ | $\eta_c$ | Internal efficiency of DC-DC converters, - |
| $I_r$ | Incidence irradiance, W/m$^2$ | $V_{in}$ | Input voltage of DC-DC converter, V |

(*continued on next column*)

(*continued*)

| Symbols | | | |
|---|---|---|---|
| N | Quality factor diode, - | ΔV | Output voltage variation of DC-DC converter, V |
| $R_s$ | Series resistance, Ohm | $P_{(ext.DC-DC)}$ | Power consumption of the DC-DC converters, W |
| $R_p$ | Parallel resistance, Ohm | $\sigma_m$ | Standard deviation of irradiance between modules, kW/m$^2$ |
| ε | Electromotive force, V | PV | Photovoltaic |
| r | Internal impedance, Ohm | DC | Direct current |
| $S_{cell}$ | Illuminated area of the cell, mm$^2$ | $N_c$ | Number of CPV cells per module |
| V | Voltage, V | $N_m$ | Number of modules in the receiver |
| $V_T$ | Thermal voltage, V | | |

(*continued on next page*)

* Corresponding author.
*E-mail address:* desideri.regany@udl.cat (D. Regany).

https://doi.org/10.1016/j.solmat.2024.113262
Received 28 June 2024; Received in revised form 24 October 2024; Accepted 29 October 2024
Available online 2 November 2024

(*continued*)

| Symbols | | | |
|---|---|---|---|
| T | Temperature, K | **Acronyms** | |
| $E_g$ | Effective energy gap, eV | MPPT | Maximum Power Point Tracking |
| $e^-$ | Electron charge, C | MPP | Maximum power point |
| $\eta_{cell}$ | CPV cell efficiency, - | DC | Direct current |
| $P_{sun}$ | Incident irradiance to the CPV cell, W | CPV | Concentrating photovoltaics |

## 1. Introduction

Central tower concentrating solar technologies can play a crucial role in integrating electricity and heat for high-temperature steam electrolysis, enhancing solar-to-electrolyzer energy efficiency [1]. Recent studies show that these technologies can supply heat for high-temperature steam electrolysis while generating electricity via thermodynamic cycles [2,3] or concentrated thermo-PV receivers [4,5]. In Solid Oxide Electrolyzers (SOECs) operating at up to 800 °C, solar heat can provide up to 28 % of the Gibbs free energy needed for electrolysis, which is more cost-effective and efficient to produce than electricity [6].

Central tower concentrating solar systems feature low-cost, scalable heliostat fields [7]. Concentrating Photovoltaics (CPV) systems, using high-efficiency PV cells, can be adapted to smaller areas without efficiency loss. However, CPV installations face challenges that need addressing for broader implementation. Lasich et al. [8] developed a business model to address these issues, demonstrating effective low-cost CPV solar energy with attractive returns on investment, even at small scales. Their approach uses a central receiver-PV architecture where the complex generation components are centralized in a small, factory-built receiver, while the collector is a commercial heliostat field. This reduces manufacturing and deployment costs significantly, making the system competitive at scales as small as 1 MW.

Solar irradiance on CPV receivers is often non-uniform due to factors such as tracking precision, time delays between heliostats, Gaussian illumination profiles [9], mirror imperfections, or structural misalignment. The current generated by a photovoltaic cell depends on incoming irradiance, and variations between cells in series cause current mismatches, limiting the overall current to that of the least irradiated cell, affecting power transfer efficiency [10]. Series connections minimize Joule-effect losses but suffer from current mismatch, while parallel connections remove current restrictions but impose a uniform voltage, leading to mismatched voltage due to varying cell temperatures. This issue aligns with the maximum power transfer theorem, which states that maximum power transfer occurs when the load impedance matches the source's internal impedance. In several studies, DC-DC converters are implemented to mitigate current mismatch by adjusting the source impedance to match between cells, even under varying irradiance conditions.

To mitigate power transfer loss from current mismatch in series connections, Eccher et al. [11] demonstrated that connecting each PV cell to a partial DC-DC converter improves power transfer efficiency by around 10 %. These converters supply only the mismatch current between the series current and the maximum power point (MPP) current of each CPV cell, enhancing overall efficiency compared to traditional converters or microinverters. This experimental study was limited to a 4-cell array (1 $cm^2$ each), but commercial CPV receivers require higher compactness [8], posing challenges for implementing dedicated DC-DC converters for each cell.

Previous studies on a 6x8 cell CPV receiver [12], found that the parallel-series configuration, with parallel cell modules equipped with DC-DC converters linked in series, yields the best output. This configuration also showed a 43.2 % improvement in power output compared to series configurations [13]. To further this, in a previous study [12] we modelled DC-DC converters numerically, considering their technical specifications and control mechanisms under six different illumination profiles.

The electrical connection between cells is crucial for achieving high packing density in the receiver design. While back-contact cells resolve surface metallization issues [14,15], only interdigitated back contact (IBT) cells have zero shading losses [16]. However, IBT cells are limited to single p-n junctions, typically silicon, with a theoretical efficiency limit of 29.43 % [17]. In multijunction solar cells, shading losses can be reduced using metal wrap-through and emitter wrap-through architectures, which route front contacts to the back, but these technologies are less developed and currently achieve lower efficiencies compared to front-contact cells, which hold the record at 47.6 % [18]. For our study, we selected commercially available multijunction PV cells with 42.8 % efficiency at 500 kW/$m^2$ and 25 °C under AM1.5D [19], featuring back metallic contacts and front bus-bar contacts.

CPV receivers also require active cooling systems with extremely low thermal resistance ($<1x10^{-4}$ $m^2K/W$) [20] to maintain high efficiency and reliability. Although microchannel-based liquid cooling systems meet this requirement, they cause voltage mismatches due to temperature variations along the channel flow path [21,22]. Various cooling geometries have been proposed to address this, including tailored-width microchannels [23,24] and self-adaptive microfluidic cells [25]. This study implements the latter, as it provides improved temperature uniformity across diverse illumination profiles [10,26], enhancing receiver reliability and efficiency while saving pumping power [27,28].

This study models the thermodynamic and electrical characteristics of a CPV receiver to evaluate its overall efficiency, focusing on designing a control system for DC-DC converters to optimize operation under varying conditions. The system was simulated to assess the energy benefits of integrating DC-DC converters with a self-adaptive microfluidic cooling system.

The paper is structured as follows: Section 2 outlines the receiver design, including electrical and thermal models and illumination profiles. Section 3 presents the receiver's characteristic curve with diodes, discusses maximum power point characteristics, and details the control methodology for DC-DC converters. Section 4 analyzes the enhanced receiver characteristic curves and results.

## 2. Modelling

### 2.1. CPV receiver design

This section outlines the technical aspects of the receiver design, focusing on electrical interconnections and the cooling system. The proposed series cell connection uses shingle-shaped mounting, which is commonly adopted by other researchers [29,30]. This method increases packing density by eliminating one bus bar from each PV cell's illuminated area [31], as shown in Fig. 1.

Fig. 1(a–c) show the receiver designed to evaluate the CPV cells' electrical output. The partial cell overlap, detailed in Fig. 1(c), places the back electrode of cell 1 above the bus bar of cell 2, creating a series connection. This shingle interconnection maintains the active area of each photovoltaic cell (5.5 × 5.5 $mm^2$) while reducing the occupied area from 5.6 × 6 $mm^2$ to 5.6 × 5.72 $mm^2$, increasing the active area ratio from 90 % to 94 %.

To facilitate electrical interconnection, different views of the CPV receiver design are presented in Fig. 1 The CPV cells are mounted and electrically connected on top of the electrically conductive elements within the cooling device, which is segmented and isolated as per the interconnection scheme (Fig. 1, b). Series connections are made by positioning cells between different segments of the cooling plate along the Y axis, while parallel connections are achieved by placing cells side by side along the X axis (Fig. 1, c). This configuration allows different voltages across the cooling plate.

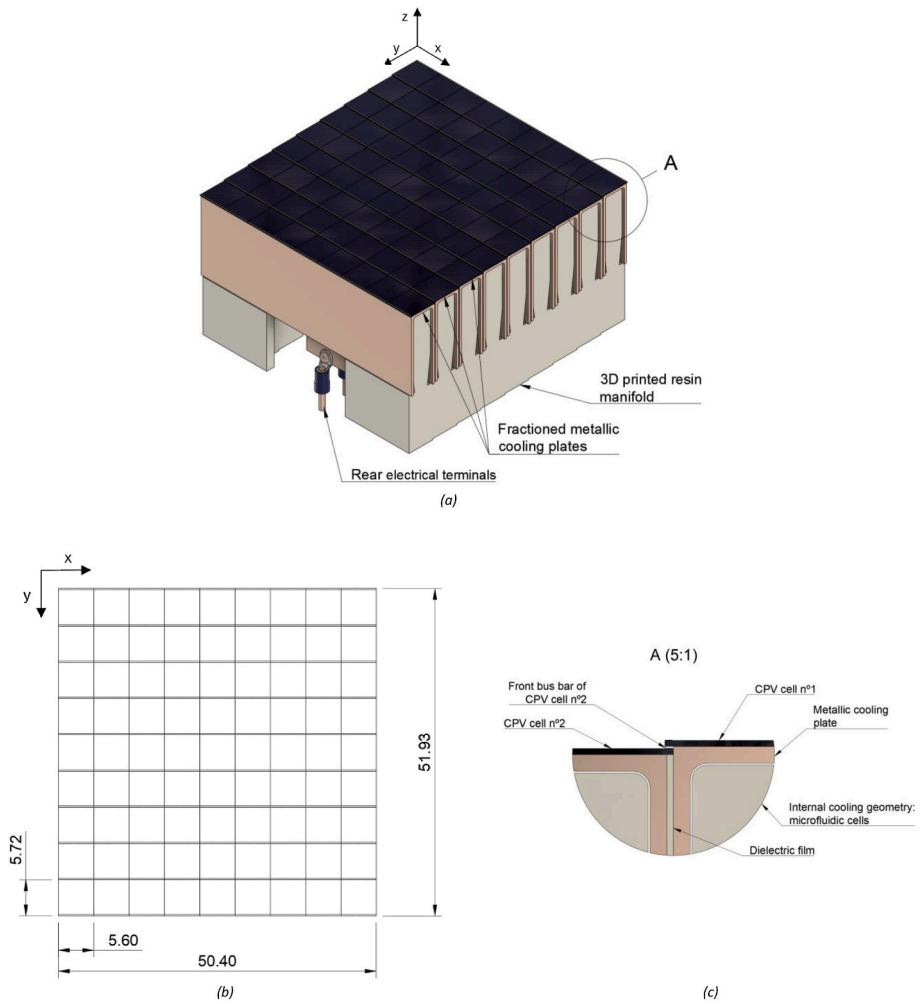


**Fig. 1.** Schematics of the dense array CPV receiver: (a) Isometric view, (b) Top view, (c) Cross-section B (units in mm).

The electrical terminals extend beyond each conductive element of the cooling plate, allowing connections with external electrical components without increasing dead space in the photovoltaic cell assembly, thus optimizing the active area ratio and enhancing energy conversion efficiency.

The cooling device's internal geometry consists of an array of microfluidic cells with individually variable coolant flow rates, as recommended by Laguna et al. [25,26], to prevent temperature non-uniformity. Each microfluidic cell (detail A in Fig. 1) self-adjusts the flow rate based on local temperature via a temperature-controlled microvalve [32]. This adjustment reduces thermal gradients and minimizes pumping consumption for cells with lower thermal demand. The microfluidic cells are supplied with cooling fluid through a manifold with multiple inlet and outlet channels located beneath the array.

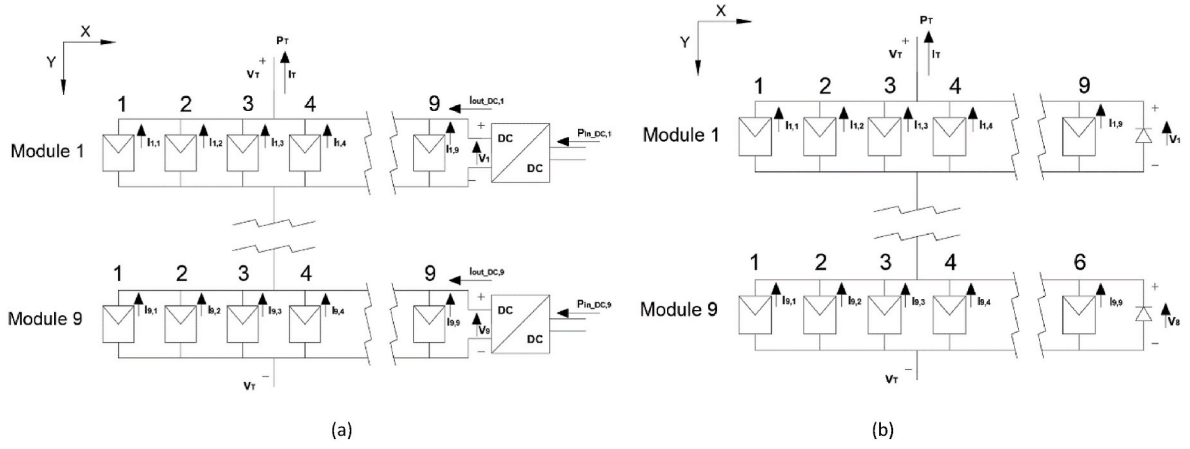


**Fig. 2.** Electrical configuration of photovoltaic cells with (a) DC-DC converters and (b) diodes.

### 2.2. CPV receiver electrical model

#### 2.2.1. Electrical interconnection

The interconnection of cells significantly impacts the power output of a multi-cell array under non-uniform illumination due to voltage and current mismatches. The 9x9 parallel-series configuration (Fig. 2) has been chosen because it is less affected by electrical mismatches compared to other configurations [10,13].

Bypass diodes are installed in parallel with each module (Fig. 2, b) to mitigate the effects of current mismatch when the average irradiance differs between modules. As the series current ($I_T$) increases, the voltage of each module decreases, can reach zero or negative values where the module's cells begin to absorb energy. However, the maximum current through the module remains close to its short-circuit current, which depends mainly on its mean irradiance, thereby limiting the series current across other modules. To address this, the bypass diodes are activated when a module's voltage becomes sufficiently negative to directly bias the diode, allowing the series current to flow without further voltage reduction.

In this study, we evaluate the energy savings achieved by replacing bypass diodes with DC-DC converters (Fig. 2, a). The primary function of the DC-DC converters is to compensate the current mismatch in the module to supply additional current to each module until the series current is reached, while maintaining the module's operating voltage at the level set by the converter, typically corresponding to the maximum power point voltage of each module.

The electrical configurations in Fig. 2 consist of an array of 9 modules connected in series, each formed by 9 photovoltaic cells in parallel, with either a converter or a diode depending on the configuration (a or b). Equations (1)–(3) define the output current and voltage of the receiver, extending these considerations to an array of $N_m$ modules in series. Each module comprises $N_c$ cells and either one DC-DC converter or one diode.

$$I_i = \sum_{j}^{N_c} I_{i,j}(V_i) + I_{DC,i}\,(V_i) \tag{1}$$

$$V_T = \sum_{i}^{N_m} V_i \tag{2}$$

$$P_T = I_T \cdot V_T \tag{3}$$

Where $I_i$ is the output current of the module $i$, $I_{i,j}$ is the output current of cell $j$ within module $i$, and $I_{DC,i}$ is the output current from the DC-DC converter connected to module $i$. The receiver voltage $V_T$ is the sum of the module voltage $V_i$ interconnected in series. Both the receiver voltage $V_T$ and series current $I_T$ depend on the external load connected to the receiver, typically the internal impedance of the maximum power point tracking system. The receiver output power, denoted as $P_T$, includes the electrical power generated by the CPV cells and the power delivered by the DC-DC converters.

#### 2.2.2. CPV cell electrical model

The electrical output of the PV cell [19] under different irradiation and temperature conditions is calculated through an 8-parameter double-diode model for a multijunction solar cell (Fig. 3) as a parallel combination of a current source, two exponential diodes and a parallel resistor, *Rp*, that are connected in series with a resistance *Rs*. The output current *I* is given by.

$$I = I_{ph} - I_s \cdot \left(e^{\frac{V+I\cdot Rs}{N_1 \cdot V_{th}}} - 1\right) - I_{s2} \cdot \left(e^{\frac{V+I\cdot R_s}{N_2 \cdot V_{th}}} - 1\right) - \frac{V + I\cdot R_s}{R_p} \tag{4}$$

Where $I_s$ and $I_{s2}$ are the diode saturation currents, $V_{th}$ is the thermal voltage, *N1* and *N2* are the quality factors (diode emission coefficients) and $I_{ph}$ is the solar-generated current. The thermal voltage $V_{th}$ is defined as the following expression:

$$V_{th} = \frac{k_B \cdot T}{e^-} \tag{5}$$

Where $k_b$ is the Boltzmann constant, $T$ is the operating cell's temperature, and $e^-$ is the electron charge.

The solar-generated current $I_{ph}$ is given by:

$$I_{ph} = I_{ph0} \cdot \left(\frac{I_r}{I_{r0}}\right) \tag{6}$$

Where $I_{ph0}$ is the measured solar-generated current for irradiance $I_{r0}$ and, $I_r$ is the incidence irradiance in $W/m^2$.

Additionally, the following Equations (7)–(11) were applied to correct the solar cell parameters that depend on temperature:

$$Iph(T) = Iph \cdot \left(1 + T_{I_{ph1}} \cdot (T - T_{meas})\right) \tag{7}$$

$$\mathrm{Is(T)} = \mathrm{Is} \cdot \left(\frac{T}{T_{meas}}\right)^{\left(\frac{TX_{IS_1}}{N1}\right)} \cdot e^{\left(E_g \cdot \frac{\left(\frac{T}{T_{meas}} - 1\right)}{N_1 \cdot V_{th}}\right)} \tag{8}$$

$$\mathrm{Is_2(T)} = \mathrm{Is_2} \cdot \left(\frac{T}{T_{meas}}\right)^{\left(\frac{TX_{IS2}}{N_2}\right)} \cdot e^{\left(E_g \cdot \frac{\left(\frac{T}{T_{meas}} - 1\right)}{N_2 \cdot V_{th}}\right)} \tag{9}$$

$$\mathrm{R_s(T)} = R_s \cdot \left(\frac{T}{T_{meas}}\right)^{T_{RS}} \tag{10}$$

$$\mathrm{R_P(T)} = R_P \cdot \left(\frac{T}{T_{meas}}\right)^{T_{RP}} \tag{11}$$

Where $T$ is the cells' temperature, $T_{meas}$ is the measurement temperature parameter, $T_{IPH1}$ is the first order temperature coefficient for $I_{ph}$. Finally, temperature exponents for $I_s$, $I_{s2}$, $R_S$, $R_P$ are $TX_{IS1}$, $TX_{IS2}$, $T_{RS}$, $T_{RS}$, respectively.

The incidence solar power is calculated in Equation (12) by multiplying incidence irradiance $I_r$ with the total illuminated area of the cell $S_{cell}$. The electrical efficiency of the PV cell $\eta_{cell}$ is calculated in Equation (14) using the input energy Equation (12) and the electrical output of the PV cell from Equation (13).

$$P_{sun} = I_r \cdot S_{cell} \tag{12}$$

$$P_{cell_{i,j}} = V_{i,j} \cdot I_{i,j} \tag{13}$$

$$\eta_{cell} = \frac{P_{cell}}{P_{sun}} \tag{14}$$

The efficiency of a single CPV cell, considering its active area (5,5 x 5,5 $mm^2$), is evaluated using the Equations (4-(14), based on the values from the CPV cell model (Table 1). This is illustrated in Fig. 4, which shows the efficiency's dependence on both temperature and irradiance.

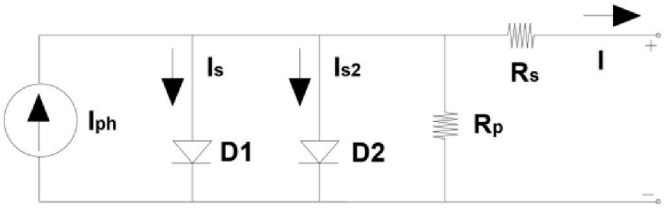


**Fig. 3.** Equivalent circuit diagram for the double-diode model of the multijunction solar cell.

**Table 1**
*Parameterized values for the 8-parameter double-diode model of AzurSpace Solar Power GmbH 3C44 - 5,5 x 5,5* $mm^2$ *CPV cell* [19] *version with grid optimized for medium concentration and antireflective coating adapted to air, available library in Matlab Simscape Electrical* [33].

| DESCRIPTION | SYMBOL | VALUE | UNITS |
|---|---|---|---|
| Diode 1 Saturation current | $I_s$ | $2.7359 \cdot 10^{-35}$ | A |
| Diode 2 Saturation current | $I_s$ | $1.1678 \cdot 10^{-37}$ | A |
| Solar-generated current for measurements | $I_{ph0}$ | 1.1900 | A |
| Irradiance used for measurements | $I_{r0}$ | $250 \cdot 10^{3}$ | $W/m^2$ |
| Diode 1 Quality factor | $N_1$ | 1.5030 | [−] |
| Diode 2 Quality factor | $N_2$ | 1.5953 | [−] |
| Series resistance | $R_s$ | 0.1043 | Ohm |
| Parallel resistance | $R_p$ | 26248.1045 | Ohm |
| First order temperature coefficient for $I_{PH}$ | $T_{IPH1}$ | $7.9999 \cdot 10^{-4}$ | 1/K |
| Energy gap | $E_g$ | 1.441 | eV |
| Temperature exponent for $I_s$ | $TX_{IS1}$ | 92.8778 | [−] |
| Temperature exponent for $I_{s2}$ | $TX_{IS2}$ | 227.9262 | [−] |
| Temperature exponent for $R_s$ | $T_{RS1}$ | $2.1642 \cdot 10^{-2}$ | [−] |
| Temperature exponent for $R_p$ | $T_{RP1}$ | 0 | [−] |
| Measurement temperature | $T_{meas}$ | 298.15 | K |

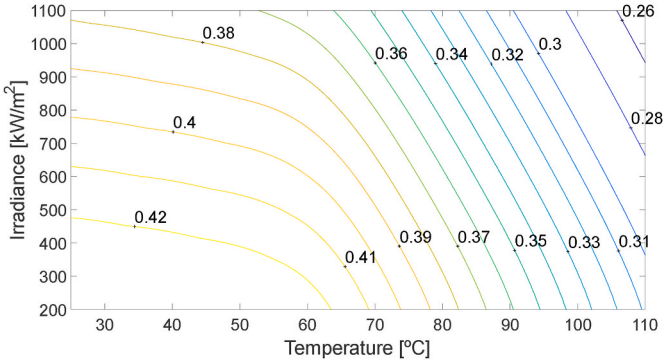


**Fig. 4.** Modelled dependence of the efficiency of the AzurSpace 3C44 CPV cell [19] *under different irradiance and temperature conditions.*

On one hand, an increase in temperature causes a rapid efficiency loss since the maximum power voltage is significantly affected by temperature, as described in Equations (5)–(9). This occurs due to the thermal voltage (Equation (5)) and the increase in reverse saturation current with temperature (Equations (8)-(9)), leading to current loss through internal recombination. On the other hand, as the model accounts for series resistance, an increase in irradiance results in a direct rise in current (Equation (6)), which causes a voltage drop, resulting in a sharp decrease in efficiency at higher irradiances.

### 2.2.3. DC-DC converter electrical model

The electrical model of the DC-DC converters is defined in Equation (15) as a linear current generator by two parameters: the electromotive force $\varepsilon_i$ and the internal resistance $r_i$. The electrical power consumed by the DC-DC converters and the net power of the receiver are defined using Equation (16)–(18).

$$V_i = \varepsilon_i - I_i r_i \tag{15}$$

$$P_{in\_DC,i} = \frac{I_i \cdot V_i}{\eta_c} \tag{16}$$

$$P_{in\_DC} = \sum_{i}^{N_m} P_{in\_DC,i} \tag{17}$$

$$P_{net} = P_T - P_{in\_DC} \tag{18}$$

Where $V_i$ is the output voltage of DC-DC converter *i,* calculated from its electromotive force $\varepsilon_i$ and the internal voltage drop due to the current $I_i$ across the internal impedance $r_i$. The term $P_{in\_DC,i}$ represents the input power supplied to each DC-DC converter, accounting for an internal efficiency ($\eta_c$) of 0.87, based on the specifications of the selected commercial DC-DC converters [34]. Finally, $P_{in\_DC}$, $P_T$ and $P_{net}$ refer to the power consumption of the DC-DC converters, total receiver power output, and net receiver power, respectively. As shown in Equation (18), the power supplied to each DC-DC converter is subtracted from the total receiver output power. The number of DC-DC converters, denoted by $N_m$, corresponds to the number of modules to DC-DC converters.

The main electrical requirements for DC-DC converters include the ability to supply output currents (0–80 A) to compensate for current mismatches between modules, an adjustable output voltage (0.6–5 V) to be tuned to each module's maximum power point, low internal impedance, and protection against overcurrent, negative current and overvoltage. These protections allow the converters to handle higher voltages when the external load is too high, even with a lower output voltage set on the converters. This ensures that the converters do not draw current from the modules under such conditions. Additionally, overcurrent protection limits the current delivered by the converters, disconnecting them when necessary to allow the receiver to operate at voltages lower than the set voltage of the DC-DC converters. Since each DC-DC converter supplies modules connected in series, an isolated power supply is required for the selected non-isolated DC-DC converters. For this study, we modelled two OmniOn Power DC-DC converters connected in parallel to meet the output specifications presented in Table 2.

The electrical modeling of the configuration with bypass diodes is based on the direct biasing of the diode when the voltage drop in a module reaches −0.5V, triggering its activation. This occurs when a current mismatch between modules reduces the electrical potential of the less productive CPV modules to negative values, causing energy absorption from the other modules and leading to hot spots. To mitigate this issue, the bypass diodes activate to limit the voltage drop to the activation threshold, allowing for higher series current and preventing further damage.

### 2.2.4. Receiver efficiency

The external energy provided to a conventional CPV receiver (Fig. 2, b) is zero. However, introducing an active element such as a DC-DC converter increases the external power demand above zero. The PV array produces a net power $P_{NET(PV\ +\ DC)}$ (Equation (20)) based on the total output power $P_T$ (Equation (19)) and the power consumption of the DC-DC converters $P_{ext.\ DC\text{-}DC}$ (Equation (12)).

The electrical efficiency of the receiver plus DC-DC converters $\eta_{receiver}$ is calculated in Equation (22) using the net electrical output and the input energy of the receiver from Equations (20) and (21), respectively. The input energy depends on the incident irradiance $I_r$ and the area of the receiver $S_{receiver}$.

$$P_T = V_T \cdot I_T \tag{19}$$

**Table 2**
Output specifications of two OmniOn Power (model NSR040A0X43Z) converters connected in parallel.

| PARAMETER | SYMBOL | MIN | TYP | MAX | UNITS |
|---|---|---|---|---|---|
| INPUT VOLTAGE | $V_{in}$ | 5 | – | 14 | V |
| OUTPUT CURRENT RANGE | $I_i$ | 0 | – | 80 | A |
| OUTPUT VOLTAGE SET POINT RANGE | $V_i$ | 0.6 | – | 5 | V |
| OUTPUT VOLTAGE VARIATION (WITHIN THE CURRENT RANGE) | ΔV | – | 0.004 | 0.010 | V |
| INTERNAL RESISTANCE | $r_0$ | – | $3.33 \cdot 10^{-5}$ | $8.33 \cdot 10^{-5}$ | Ω |
| EFFICIENCY | η | – | 87 | 90 | % |

$$P_{NET(PV+DC)} = P_T - P_{ext.\ DC-DC} \tag{20}$$

$$P_{sun} = I_r \cdot S_{receiver} \tag{21}$$

$$\eta_{receiver} = \frac{P_{NET(PV+DC)}}{P_{sun}} \tag{22}$$

### 2.3. Illumination profiles

This section presents the illumination profiles (Fig. 5) considered to assess the impact of DC-DC converters on the electrical output of the receiver. These profiles are identified to cover the majority of situations encountered during normal operation of the CPV receivers [26].

Since the photogenerated current in a CPV cell is proportional to the incident irradiance (Equation (6)), illumination non-uniformities between modules result in a current mismatch when connected in series, leading to power loss. To quantify the power transfer loss due to these non-uniformities, the standard deviation of the average irradiance between modules ($\sigma_m$, Equation (23)) is evaluated.

$$\sigma_m = \sqrt{\frac{\sum_{i=1}^{N_m} (R_{Si} - \overline{R_S})^2}{(N_m - 1)}} \tag{23}$$

Where $R_{Si}$ is the mean solar irradiance of the module $i$, $N_m$ is the total number of modules, and $\overline{R_S}$ is the mean irradiation on the entire CPV receiver (800 kW/m$^2$).

### 2.4. Thermal modelling

The illumination profiles impact the operating temperature of the cells, primarily depending on the heat extraction capacity of the cooling device and the coolant inlet temperature, fixed at 20 °C. The operating temperatures of the cells are calculated using Equation (24) as a numerical interpolation of the thermodynamic model results performed by Fernández et al. [35] employing a finite element solver (COMSOL) for the microfluidic cells cooling device [27,28], with a mean squared error of 1.27 %.

$$T = a \cdot e^{(b \cdot \dot{q})} + d \cdot e^{(e \cdot \dot{q})} + (T_{coolant} - 30) \tag{24}$$

Where $T$ refers to the temperature of the photovoltaic cell [K], $T_{coolant}$ to the inlet temperature of coolant [K], $\dot{q}$ to the heat flux density [kW/m$^2$] and the coefficients $a$, $b$, $d$, $e$ to the values 352.12 [K], 1.28·10$^{-2}$ [m$^2$/kW], −21.92 [K], −0.003 [m$^2$/kW], respectively. The pumping consumption is subtracted from the electrical production to obtain the net output power of the receiver, calculated based on the microfluidic cell hydraulic power as described by Fernández et al. [35].

Additionally, to determine the operating temperature of the photovoltaic cell, it is essential to consider that under normal conditions, the cells convert irradiance into electrical energy, thereby reducing the energy converted to heat. For thermal modelling, a numerical model solves the energy balance of a CPV cell presented in Equation (25) using an iterative numerical method (Bolzano) to find the root of the near-zero error objective function, ensuring it is below 1 mW (0.008 % of the maximum power point of the CPV cell under standard conditions).

$$P_{sun} = P_{cell} + \dot{q} \cdot S_{cell} \tag{25}$$

Where $P_{sun}$ is the incidence solar power, $P_{cell}$ is the electrical power generated by the CPV cell, considering its illuminated area $S_{cell}$ and the heat flux density $\dot{q}$. By applying the energy balance between absorbed irradiance, generated electrical power, and dissipated thermal heat flux, the operating temperature of the CPV cell is calculated based on its operating voltage, as shown in Fig. 6.

Fig. 6 distinguishes three operating regions based on the CPV cell's voltage range. The electrically non-productive region (right) occurs

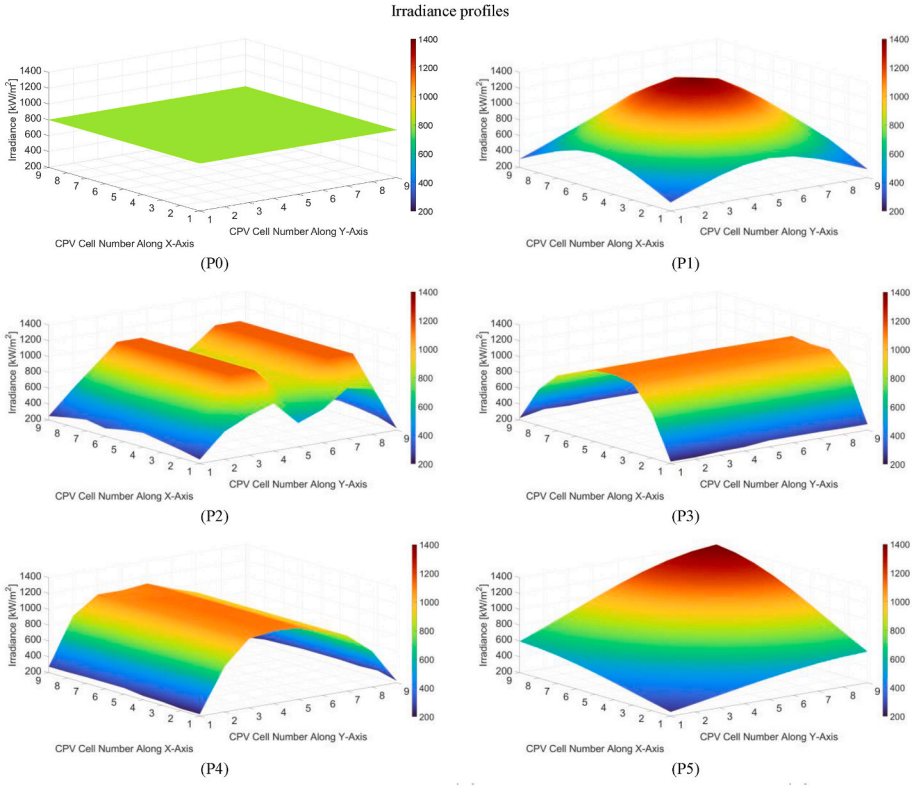


**Fig. 5.** Illumination distribution across CPV receiver surface. P0: Uniform ($\sigma_m$ = 0 kW/m$^2$), P1: Gaussian 1 central maximum ($\sigma_m$ = 217 kW/m$^2$), P2: Gaussian 2 maximums ($\sigma_m$ = 312 kW/m$^2$), P3: dispersion within module ($\sigma_m$ = 8 kW/m$^2$), P4: large dispersion between modules ($\sigma_m$ = 339 kW/m$^2$), P5: off-axis illumination ($\sigma_m$ = 220 kW/m$^2$).

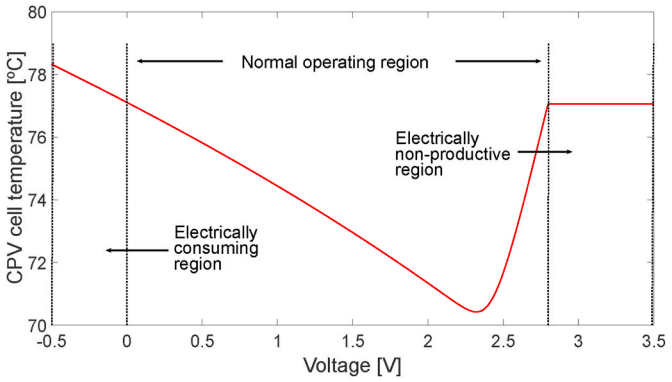


**Fig. 6.** Evolution of the calculated CPV cell temperature as a function of operating voltage, under active microfluidic cooling, when subjected to 800 kW/m$^2$ of irradiance.

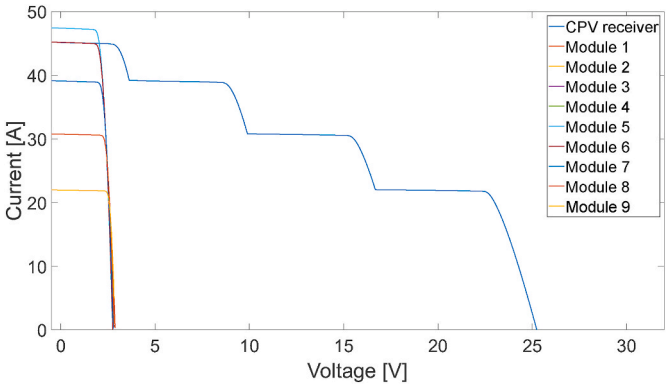


**Fig. 7.** I-V characteristic curves of the CPV receiver for illumination profile P1 (central maximum). Each module separately and the complete receiver.

when the cell current stops as voltage reaches or exceeds the open-circuit voltage, leading to reverse bias of the CPV cell. This halts the current, and the entire irradiance is dissipated as heat, maintaining the cell temperature. In the normal operation region (center), the temperature varies with electrical power generation, with the minimum temperature at the cell's maximum power point voltage. The power consumption region (left) occurs when the cell's operating voltage becomes negative, as the series current exceeds the cell's short-circuit current. This current mismatch generates excess heat, raising the cell temperature until the voltage reaches −0.5V, activating the bypass diode. Once forward biased, the diode diverts some excess current, preventing further voltage drops and limiting thermal dissipation.

### 2.5. I-V characteristic curve of CPV array with diodes

The electrical behaviour of the CPV dense array formed by 9x9 parallel-series configuration shown in Fig. 2(b), with the use of bypass diodes instead of DC-DC converters, is analysed when the receiver is subjected to the Gaussian 1 central maximum profile, shown in Fig. 5 (P1).

The electrical production of each CPV cell is calculated using the model described in Section 2.2.2, which depends on the parameters of incident irradiance and operating temperature. The operating temperature is determined by considering the energy balance between the incident irradiance, the generated electrical power, and the thermal power extracted for the cooling system, according to its thermodynamic model (Section 2.4). The energy balance involves solving a model with transcendental equations, requiring numerical methods.

Once the operating parameters are determined, the electrical behavior of the receiver can be evaluated, considering the intrinsic constraints of the electrical configuration. The operating characteristic curves of each module of cells are obtained by summing the current of each cell (Equation (*4*)) as a function of the parallel connection voltage (as *V* in Section 2.2.2). The characteristic curve of the receiver is then calculated by considering the series association of the 9 modules. The final voltage is obtained by adding the voltages of each module (Equation (*2*)) as a function of the receiver output current (Equation (*1*)).

The I-V characteristics curve of the receiver for illumination profile P1 is shown in Fig. 7 (labeled as "CPV receiver"). Additionally, the figure shows the characteristic curves of the 9 modules working individually under the illumination conditions that spatially occur in the receiver.

Fig. 7 illustrates the staggered behavior of the receiver's I-V characteristic curve, caused by differences in average irradiance between the modules and the activation of the bypass diodes as the impedance connected to the receiver decreases. When the receiver's output current exceeds the short-circuit current of one of the modules, the affected module's cells begin to absorb energy, driving its operating voltage to negative values. This staggered behavior occurs when a module reaches a sufficiently negative voltage to directly bias its bypass diode, allowing the series current to flow without further reducing the module's voltage. Since Profile 1 applies similar mean irradiance to multiple modules, the generated current values are close, causing some I-V curves of the modules to overlap.

### 2.6. Maximum power point characteristics of CPV cells and modules

The characteristics of the maximum power point of each photovoltaic cell and module, working independently of the electrical configuration, are considered for the illumination profile P1 and the operating temperature according to the energy balance and the cooling system model.

Fig. 8 show the voltage, current, and power values that determine the operating conditions of the maximum power point of each module as a function of the concentration ratio.

Fig. 8 illustrates the relationship between the maximum power point parameters —current, voltage, power, and temperature— as a function of the mean irradiance for each module in the CPV receiver. As expected, the current increases linearly with irradiance, reflecting the direct relationship between irradiance and photocurrent generation in the CPV cells. However, the voltage exhibits a slight decrease, which can be attributed to two main factors. First, the increased irradiance raises the operating temperature of the CPV cells, as shown in the temperature profile. This temperature rise reduces the open-circuit voltage, subsequently lowering the MPP voltage. Second, series resistance losses within the cells increase with irradiance, further reducing the MPP voltage.

These combined factors result in a reduction in MPP voltage and overall system efficiency at higher irradiance levels, leading to the logarithmic trend observed in the power regression curve. This

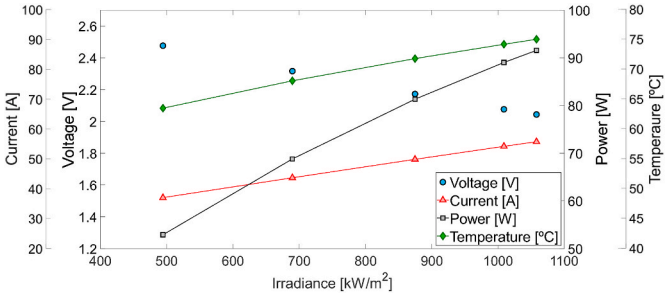


**Fig. 8.** Values of maximum power point parameters (voltage, current, and power) of each module in the CPV receiver as a function of the mean irradiance. The illumination profile used is P1.

highlights the importance of efficient thermal management and minimizing resistive losses, especially when operating at high irradiance levels.

## 3. Results

This section examines the control of the DC-DC converters to compute and analyze the electrical behavior of the CPV receiver in terms of power transfer efficiency with DC-DC converters (Fig. 2a) and with diodes (Fig. 2b) for each of the previously defined illumination profiles (Fig. 5).

The electrical simulation of the CPV receiver is conducted numerically using MATLAB, integrating the thermal and electrical models of the system. The thermal model calculates the operating temperature of the PV cells using the thermodynamic model of the microfluidic cells cooling device [10,36], considering the energy balance between irradiance and electrical output. The electrical model includes the specifications of both the commercial DC-DC converters and PV cells selected, as well as the electrical constraints of the 6x8 parallel-series PV cells configuration in the receiver.

### 3.1. Control of DC-DC converters

The selected DC-DC converters exhibit a high degree of ideality as current sources, ensuring voltage stability across a wide range of current levels (Fig. 9).

This characteristic is particularly advantageous in preventing voltage and power loss as the current mismatch increases. Additionally, equipped with safeguards against negative currents and overpotentials, each DC-DC converter can operate within a voltage range from the module's open-circuit voltage to beyond the maximum power voltage as the impedance connected to the receiver decreases. Upon reaching the setpoint voltage of the DC-DC converter, each module supplies the current mismatch according to its internal impedance, preventing voltage reduction as receiver current rises. Furthermore, the selected DC-DC converters offer the flexibility to adjust the setpoint voltage within a 0.6–5 V range to match the maximum power point of each module, responding to changes in both CPV cells, ambient temperature and cooling plate characteristics.

The DC-DC control methodology employs two Maximum Power Point Tracking (MPPT) algorithms. The first algorithm adjusts the voltage of all DC-DC converters, while the second modifies the output impedance of the CPV receiver by adjusting it to maximize the net output power at that specific DC-DC converter voltage, similar to approaches described in intelligent MPPT methods such as Fuzzy Logic Control [38]. After determining the net output power associated with that voltage, the first MPPT algorithm selects the next voltage for the DC-DC converters setting to further optimize the receiver efficiency, ensuring that the system operates at maximum power, as illustrated in Fig. 10.

Fig. 10 illustrates the receiver's efficiency curve at its maximum power point as a function of the voltage applied by the DC-DC converters, which refers to the biasing voltage applied to each corresponding module. As the voltage of the DC-DC converters decreases from the maximum power point, the module voltage drops to that voltage before allowing the series current to exceed the module's current. When the DC-DC converter voltage is reduced to −0.5V, the module operates similarly to the diode configuration, permitting current flow while contributing to power consumption. However, the overall efficiency remains above 0 % because only the less productive modules are biased at such low voltages, while the more productive modules continue operating at higher voltages depending on the series current. As the voltage bias decreases, the I-V curve becomes more staggered, but the receiver's overall efficiency remains positive since not all modules contribute zero power.

This behavior is further explored in Figs. 11 and 12, where the I-V and P-V curves show that the receiver's maximum power point occurs at a lower voltage with diodes than with DC-DC converters. The detailed DC-DC converter control algorithm enables the system to self-converge to optimal operating conditions for all modules, even under varying ambient temperatures, cooling capacities, and illumination conditions. This feature, as demonstrated by the results in subsequent sections, significantly improves the applicability and reliability of the mismatch loss reduction system.

### 3.2. Comparison of I-V characteristic curves

This subsection analyzes the receiver output current $I_T$ presented in Fig. 9 through the I-V characteristic curves for the electrical configuration with diodes (PV) and with DC-DC converters (PV + DC) according to the illumination profile to which the receiver is subjected.

In the dotted curves of subsections P1, P2, P4 and P5 in Fig. 11, it can be observed that as the current $I_{PV}$ increases, the receiver voltage decreases until the least productive module losses all its voltage and reaches −0.5 V, activating its bypass diode. Consequently, the module's short-circuit current stops restricting the series current, which continues to increase but at the cost of consuming energy from the other modules.

To address this issue, the DC-DC converters supply the current mismatch relative to the series current when the module voltage reaches

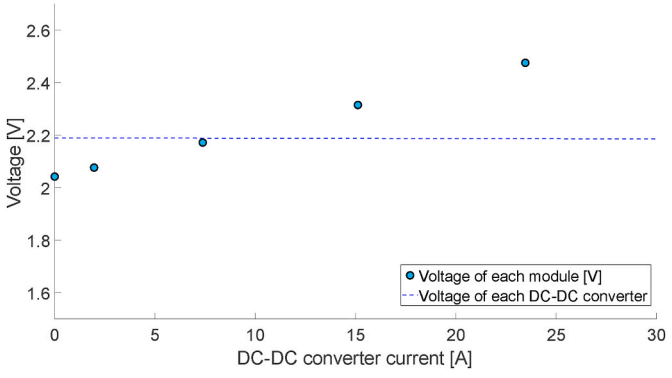


**Fig. 9.** Maximum power voltage values of each module of the CPV receiver as a function of the current delivered by the DC-DC converters for illumination profile P1.

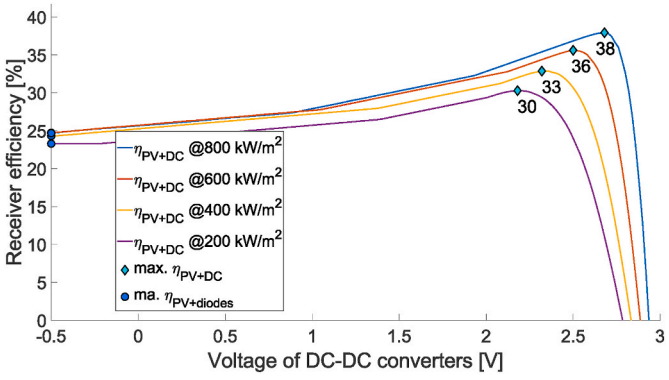


**Fig. 10.** Receiver efficiency plotted against the voltage of the DC-DC converters, representing the maximum power point of the receiver using DC-DC converters or diodes at different mean receiver irradiance levels under a Gaussian profile P1.

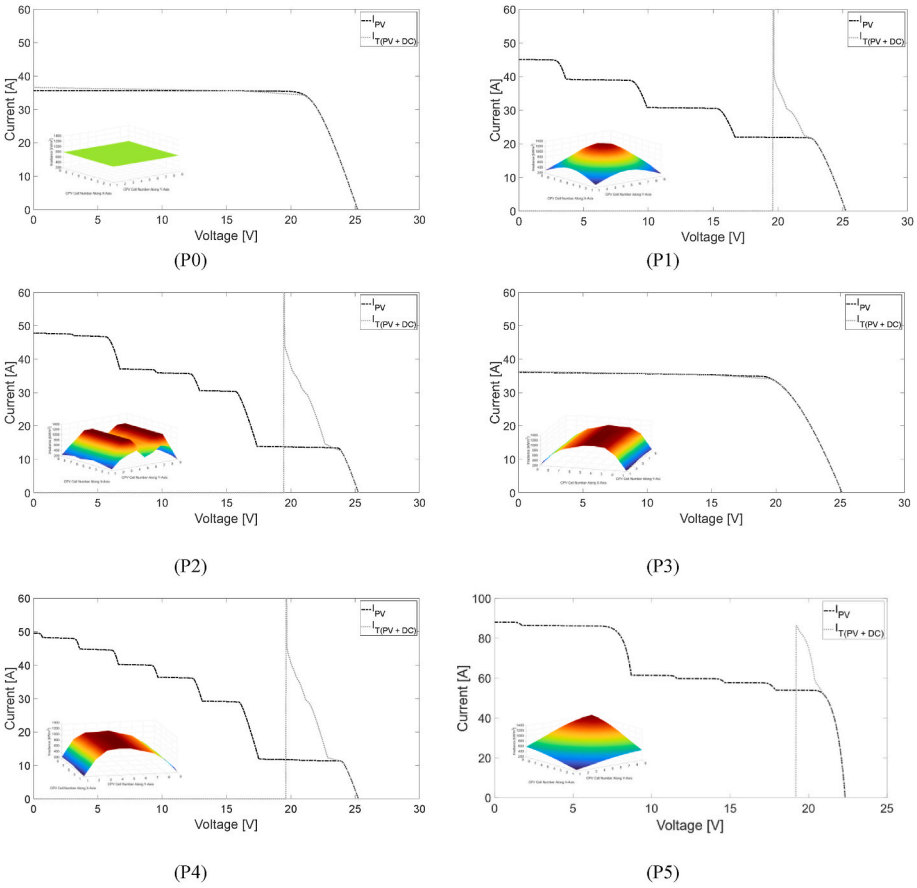


**Fig. 11.** I-V characteristic curves of the CPV receiver for several illumination profiles. P0: Uniform, P1: 1 central maximum, P2: 2 maximums, P3: dispersion within modules, P4: large dispersion between modules, P5: off-axis illumination. Total output current of the receiver using bypass diodes or with DC-DC converters according to the type of line dash-dot or dotted, respectively.

2.4V, set as closest to the module's maximum power point. When this occurs ($I_{T(PV\ +\ DC)}$ curve in Fig. 11), the DC-DC converter applies an almost constant operating voltage, keeping the modules close to the voltage of their maximum power point. This allows the PV cells to operate under optimal conditions despite irradiance deviations. Due to the DC-DC converters' overpotential protections, the receiver characteristic curve develops over the current range from 0 A (open-circuit condition) to the current of the maximum power point corresponding to the receiver voltage of 19.2V (lower voltage limit).

In Fig. 11(P0), it is evident that there is no difference in performance between the use of bypass diodes and the application of DC-DC converters. This results from the uniformity of the illumination profile, subjecting all the cells to the same conditions. This scenario serves as a reference since all modules deliver the same current, resulting in maximum power transfer.

A similar situation is observed in Fig. 11(P3), even though the receiver is subjected to a non uniform profile between modules (Fig. 5 (P3)). The reason is that the average irradiance is identical for each module. As a result, each module produces the same current, so the DC-DC converters remain inactive. However, this profile may cause a voltage mismatch within each module due to the temperature gradient between photovoltaic cells. This mismatch has a slight effect due to the use of the microfluidic cells cooling device.

### 3.3. Comparison of P-V characteristic curves and receiver efficiency

To evaluate the improvement in receiver efficiency using DC-DC converters, the power-voltage characteristic curves of both electrical configurations are shown in Fig. 12, with subsections corresponding to the different illumination profiles applied to the CPV receiver.

These P-V curves result from multiplying the total output voltage by the current of the receiver from previous I-V characteristic curves. The results depend on whether the modules are connected with bypass diodes $P_{PV}$ or with DC-DC converters $P_{T(PV\ +\ DC)}$, respectively.

To compare the performance improvement of the receiver with the DC-DC converters, it is necessary to subtract the consumption of the DC-DC converters from the total power value $P_{T(PV\ +\ DC)}$ (Equation *(20)*). The result is the power-voltage curve $P_{NET(PV\ +\ DC)}$, which refers to the net output power of the CPV receiver. The efficiency of the DC-DC converters is assumed to be constant at 87 % according to the device data sheet (Table 2).

Fig. 12 shows the scaled behavior of the receiver P-V characteristic curves as the receiver load impedance decreases, either with diodes or DC-DC converters configurations. On the one hand, the power curves for the diode configuration ($P_{PV}$ curves) suffer a significant maximum power loss since the maximum power voltage of the receiver is reduced, in some cases, to values below 15 V due to the rapid decrease of the operating voltage of the less productive modules.

On the other hand, the configuration with DC-DC converters ($P_{T(PV\ +\ DC)}$ curves) achieves much higher maximum power because all the modules are operating above the maximum power voltage over the entire current range of the receiver. However, as the receiver current increases, the current mismatch of the less productive modules gradually rises, resulting in a higher power demand from the DC-DC converters. Considering that these devices have an efficiency of 87 % [34], a higher demand implies higher power loss. This dissipated power corresponds to the difference between the $P_{T(PV\ +\ DC)}$ and $P_{NET(PV\ +\ DC)}$ curves, which is higher for illumination profiles with larger deviation

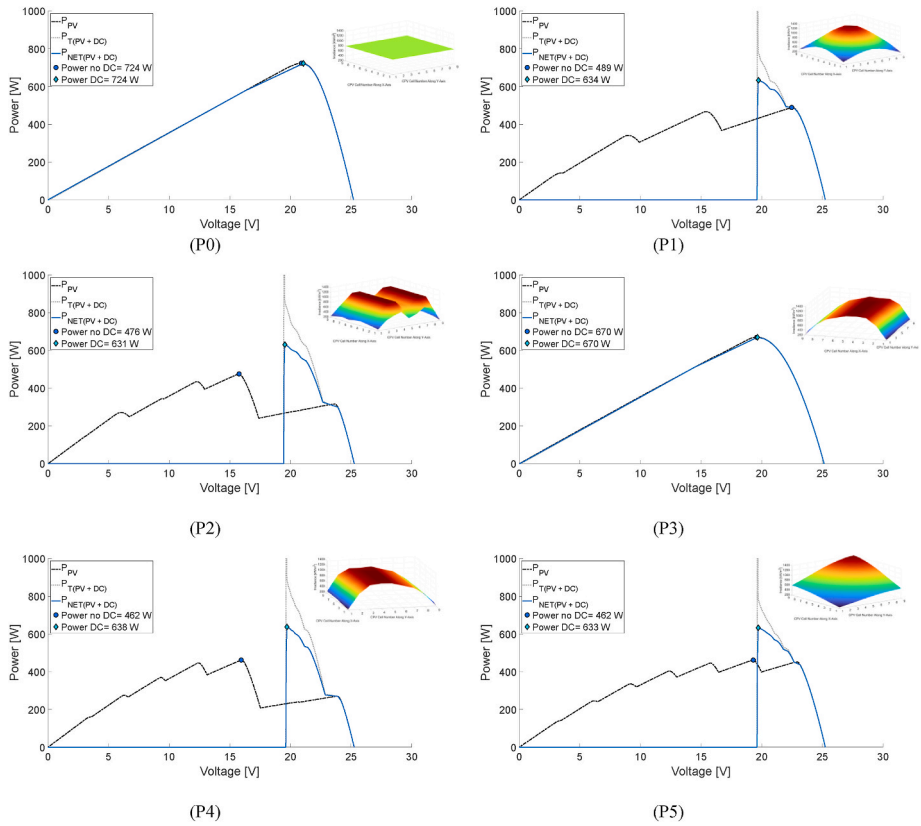


**Fig. 12.** P-V characteristic curves of the CPV receiver for several illumination profiles. P0: Uniform, P1: 1 central maximum, P2: 2 maximums, P3: dispersion within modules, P4: large dispersion between modules, P5: off-axis illumination. Total output power of the receiver with bypass diodes or with DC-DC converters is represented by dash-dot or dotted lines, respectively. The net output power with implemented DC-DC converters is represented by a continuous line.

(illumination profiles *P1* and *P4*).

To quantitatively evaluate the energy improvement of the proposed solution, Table 3 shows the net power and efficiency values of the entire receiver for the electrical configuration with diodes (*PV*) and with DC-DC converters (*PV + DC*).

The increase in receiver efficiency shown in the last row of Table 3 is attributed to the gain in power transfer efficiency resulting from the application of DC-DC converters instead of the bypass diodes configuration for each of the illumination profiles. The receiver efficiency is increased from 23.4 % to 30.3 % under Gaussian 1 central maximum profile (*P1*, $\sigma_m = 217$ kW/m2), reaching up to 38 % relative efficiency improvement under the large dispersion between modules profile (*P4*, $\sigma_m = 339$ kW/m2).

### 3.4. Power transfer losses

The power transfer loss is calculated from Equation *(26)* based on the percentage decrease in receiver output power when it is subjected to each of the illumination profiles, compared to profile 0. Profile 0 is selected as a maximum power scenario since its uniform irradiance prevents electrical mismatches between PV cells.

$$\eta_{losses} = \frac{P_{P0} - P_{Pk}}{P_{P0}} \cdot 100 \tag{26}$$

Where *k* refers to the illumination profiles ($k = 1$ to 5) and $P_{P0}$ and $P_{Pk}$ are the net output power of the receiver for profile *0* and profile *k*, respectively.

As a result, Fig. 13 presents the power transfer losses as a function of the irradiance deviation between modules ($\sigma_m$, Equation (23)), demonstrating the power improvement achieved by using DC-DC converters.

The slope of the power transfer losses shows an irradiance deviation

**Table 3**
Net output power and efficiency of the CPV receiver with bypass diodes (PV) or with DC-DC converters (PV + DC) according to the illumination profile P0 - P5 shown in Fig. 4.

| Profile | P0 | P1 | P2 | P3 | P4 | P5 |
|---|---|---|---|---|---|---|
| $P_{PV}$ [W] | 724.1 | 489.3 | 476.0 | 670.4 | 462.2 | 462.1 |
| $P_{NET\ (PV\ +DC)}$ [W] | 724.0 | 633.5 | 631.4 | 670.3 | 637.6 | 632.9 |
| $\eta_{PV}$ [%] | 34.6 | 23.4 | 22.7 | 32.0 | 22.1 | 22.1 |
| $\eta_{NET\ (PV\ +DC)}$ [%] | 34.6 | 30.3 | 30.1 | 32.0 | 30.4 | 30.2 |
| $\eta_{ratio\ (PV\ respect\ to\ PV\ +\ DC)}$ [−] | 1.0 | 1.29 | 1.33 | 1.00 | 1.38 | 1.37 |

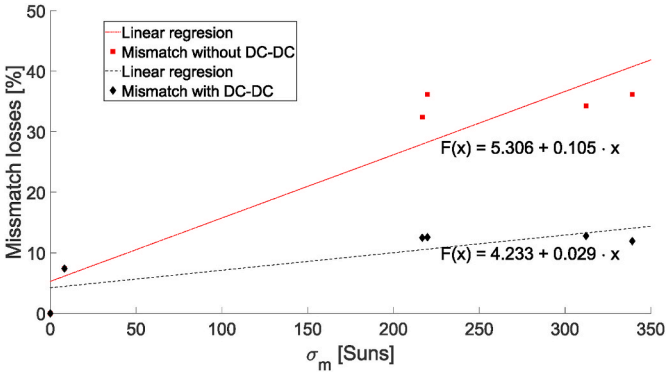


**Fig. 13.** Mismatch losses using bypass diodes or DC-DC converters for different illumination profiles as a function of the standard deviation of the mean irradiation between modules.

dependency of only 2.9 % with DC-DC converters, compared to 10.5 % in the bypass diodes configuration. According to the regression curve, when 200 kW/m$^2$ of illumination non-uniformity occurs, the power transfer losses decrease from 26 % to 10 %. This demonstrates the significant improvement with DC-DC converters, as the receiver's electrical output is significantly decoupled from the electrical constraints caused by the illumination non-homogeneities.

## 4. Conclusions

This study presents a comprehensive evaluation of a CPV receiver design that incorporates DC-DC converters and self-adaptive microfluidic cooling systems to mitigate the effects of current mismatch and temperature variations. Implementing DC-DC converters in parallel-series configurations of CPV cells significantly enhances power transfer efficiency. The receiver's efficiency improved from 23.4 % to 30.3 % under Gaussian 1 central maximum profile, with up to 38 % relative efficiency gain under large dispersion profiles.

The self-adaptive microfluidic cooling system effectively maintains uniform cell temperatures, enhancing overall receiver reliability and reducing thermal gradients that cause voltage mismatches. The proposed receiver design demonstrated a substantial increase in net output power, reaching up to 724 W under uniform illumination and maintaining high efficiency under various non-uniform illumination profiles.

The integration of commercially available multijunction PV cells with DC-DC converters and microfluidic cooling is both scalable and practical for large-scale implementations. The patented design ensures the scalability and practicability of electrical connections between the DC-DC converters and each CPV cell without creating shaded areas, optimizing the active area ratio and enhancing energy conversion efficiency.

The selected DC-DC converters exhibit a high degree of ideality as current sources, ensuring voltage stability across a wide range of current levels. Equipped with safeguards against negative currents and overpotentials, each DC-DC converter can operate within a voltage range from the module's open-circuit voltage to beyond the maximum power voltage as the receiver output impedance decreases. The control methodology employs two Maximum Power Point Tracking (MPPT) algorithms: one to adjust the voltage of all DC-DC converters and the other to modify the output impedance of the CPV receiver. This enables the system to self-converge to optimal working conditions for all PV cells, even under varying ambient temperature, cooling capacity, and illumination conditions, significantly enhancing the system's applicability and reliability.

In conclusion, the integration of DC-DC converters and advanced cooling techniques in CPV systems represents a significant advancement in solar energy technologies, addressing key challenges and paving the way for higher efficiency and more reliable solar power generation systems.

## CRediT authorship contribution statement

**Desideri Regany:** Writing – original draft, Visualization, Software, Methodology, Investigation, Funding acquisition, Formal analysis, Data curation, Conceptualization. **Francesc Majós Palau:** Software, Investigation, Data curation. **Alicia Crespo:** Methodology, Data curation. **Jérôme Barrau:** Writing – review & editing, Validation, Project administration, Methodology. **Montse Vilarrubí:** Validation. **Joan Rosell-Urrutia:** Writing – review & editing, Supervision, Methodology, Funding acquisition, Formal analysis, Conceptualization.

## Declaration of competing interest

The authors declare the following financial interests/personal relationships which may be considered as potential competing interests: Desideri Regany reports financial support was provided by Spain Ministry of Science and Innovation. Alicia Crespo reports financial support was provided by Government of Catalonia. Alicia Crespo reports financial support was provided by European Commission. Montse Vilarrubi reports was provided by European Commission. Desideri Regany has patent #EP24382230.1 pending to University of Lleida. Jerome Barrau has patent #EP24382230.1 pending to University of Lleida. Joan Rosell-Urrutia has patent #EP24382230.1 pending to University of Lleida. If there are other authors, they declare that they have no known competing financial interests or personal relationships that could have appeared to influence the work reported in this paper.

## Acknowledgements

This publication is part of the R&D grant TED2021-131580B-I00 funded by MCIN/AEI/10.13039/501100011033 and by the European Union NextGenerationEU/PRTR; and also is part of the project name: SOLARX; grant number: 101084158 funded by the European Union under the Horizon Europe Framework Programme. Views and opinions expressed are those of the author(s) and do not necessarily reflect those of the European Union or the European Climate, Infrastructure and Environment Executive Agency (CINEA). Neither the European Union nor the granting authority can be held responsible for them. The project is also supported by the Swiss State Secretariat for Education, Research and Innovation (SERI). The author Alicia Crespo is a Serra Húnter Fellow.

## Data availability

Data will be made available on request.

## References

[1] I. Dincer, C. Zamfirescu, Hydrogen and fuel cell systems. Advanced Power Generation Systems, 2014, pp. 143–198, https://doi.org/10.1016/b978-0-12-383860-5.00004-3.
[2] N. Monnerie, H. von Storch, A. Houaijia, M. Roeb, C. Sattler, Hydrogen production by coupling pressurized high temperature electrolyser with solar tower technology, Int. J. Hydrogen Energy 42 (19) (2017) 13498–13509, https://doi.org/10.1016/j.ijhydene.2016.11.034.
[3] M. Lin, S. Haussener, Techno-economic modeling and optimization of solar-driven high-temperature electrolysis systems, Sol. Energy 155 (2017) 1389–1402, https://doi.org/10.1016/j.solener.2017.07.077.
[4] H. Zhang, S. Su, X. Chen, G. Lin, J. Chen, Configuration design and performance optimum analysis of a solar-driven high temperature steam electrolysis system for hydrogen production, Int. J. Hydrogen Energy 38 (11) (2013) 4298–4307, https://doi.org/10.1016/j.ijhydene.2013.01.199.
[5] R. Daneshpour, M. Mehrpooya, Design and optimization of a combined solar thermophotovoltaic power generation and solid oxide electrolyser for hydrogen production, Energy Convers. Manag. 176 (September) (2018) 274–286, https://doi.org/10.1016/j.enconman.2018.09.033.
[6] K. Harrison, R. Remick, G.D. Martin, A. Hoskin, Hydrogen production: fundamentals and case study summaries. Hydrogen Production: Fundamentals and Case Study Summaries, 2010.
[7] M. Wiesenfarth, H. Helmers, S.P. Philipp, M. Steine, A.W. Bett, Advanced concepts in concentrating photovoltaics (CPV). 27th European Photovoltaic Solar Energy Conference and Exhibition, 2012, pp. 11–15, https://doi.org/10.4229/27thEUPVSEC2012-1AP.1.4. SEPTEMBER.
[8] J. Lasich, et al., Central receiver photovoltaics - a new generation of solar power, AIP Conf. Proc. 2012 (2018), https://doi.org/10.1063/1.5053495.
[9] G. Johnston, Focal region measurements of the 20 m2 tiled dish at the Australian National University, Sol. Energy 63 (2) (1998) 117–124, https://doi.org/10.1016/S0038-092X(98)00041-3.
[10] Á. Fernández, et al., Assessment of the impact of non-uniform illumination and temperature profiles on a dense array CPV receiver performance, Sol. Energy 171 (July) (2018) 863–870, https://doi.org/10.1016/j.solener.2018.07.001.
[11] M. Eccher, A. Salemi, S. Turrini, R.S. Brusa, Measurements of power transfer efficiency in CPV cell-array models using individual DC-DC converters, Appl. Energy 142 (2015) 396–406, https://doi.org/10.1016/j.apenergy.2014.12.038.
[12] Á. Fernández, et al., Impact of DC-DC converters on the energy performance of a dense concentrator PV array under nonuniform irradiance and temperature profiles, Energies (Basel) 17 (5) (Mar. 2024), https://doi.org/10.3390/en17051235.
[13] F.L. Siaw, K.K. Chong, A systematic method of interconnection optimization for dense-array concentrator photovoltaic system, Sci. World J. 2013 (July 2015) (2013), https://doi.org/10.1155/2013/275169.

[14] M. De Lafontaine, et al., Impact of via hole integration on multijunction solar cells for through cell via contacts and associated passivation treatment, IEEE J. Photovoltaics 7 (5) (2017) 1456–1461, https://doi.org/10.1109/JPHOTOV.2017.2711423.
[15] O. Richard, A. Jaouad, B. Bouzazi, R. Arès, S. Fafard, V. Aimez, Simulation of a through cell via contacts architecture for HCPV multi-junction solar cells, Sol. Energy Mater. Sol. Cell. 144 (2016) 173–180, https://doi.org/10.1016/j.solmat.2015.08.032.
[16] M.K. Mat Desa, et al., Silicon back contact solar cell configuration: a pathway towards higher efficiency, Renew. Sustain. Energy Rev. 60 (2016) 1516–1532, https://doi.org/10.1016/j.rser.2016.03.004.
[17] A. Richter, M. Hermle, S.W. Glunz, Reassessment of the limiting efficiency for crystalline silicon solar cells, IEEE J. Photovoltaics 3 (4) (2013) 1184–1191, https://doi.org/10.1109/JPHOTOV.2013.2270351.
[18] F. Dimroth, Fraunhofer ISE develops the world's most efficient solar cell with 47.6 percent efficiency [Online]. Available: https://www.ise.fraunhofer.de/en/press-media/press-releases/2022/fraunhofer-ise-develops-the-worlds-most-efficient-solar-cell-with-47-comma-6-percent-efficiency.html. (Accessed 22 October 2024).
[19] Azurspace Solar Power GMBH, "Concentrator Triple Junction Solar Cell. Cell Type: 3C44 – 5,5 x 5,5mm$^2$. Application: Concentrating Photovoltaic (CPV) Modules" Accessed: May 14, 2024. [Online]. Available: https://www.azurspace.com/.
[20] A. Royne, C.J. Dey, D.R. Mills, Cooling of photovoltaic cells under concentrated illumination: a critical review, Sol. Energy Mater. Sol. Cell. 86 (4) (2005) 451–483, https://doi.org/10.1016/j.solmat.2004.09.003.
[21] G. Mittelman, A. Kribus, A. Dayan, Solar cooling with concentrating photovoltaic/thermal (CPVT) systems, Energy Convers. Manag. 48 (9) (2007) 2481–2490, https://doi.org/10.1016/j.enconman.2007.04.004.
[22] I. Antón, et al., The PV-FIBRE concentrator: a system for indoor operation of 1000X MJ solar cells, Prog Photovolt 15 (2007) 431–447.
[23] S. Riera, J. Barrau, J.I. Rosell, M. Omri, L.G. Fréchette, Experimental demonstration of a tailored-width microchannel heat exchanger configuration for uniform wall temperature, J. Phys. Conf. Ser. 476 (1) (2013), https://doi.org/10.1088/1742-6596/476/1/012075.
[24] E.M. Abo-Zahhad, S. Ookawara, A. Radwan, A.H. El-Shazly, M.F. El-Kady, M.F. C. Esmail, Performance, limits, and thermal stress analysis of high concentrator multijunction solar cell under passive cooling conditions, Appl. Therm. Eng. 164 (2020) 114497, https://doi.org/10.1016/j.applthermaleng.2019.114497.
[25] G. Laguna, et al., Distributed and self-adaptive microfluidic cell cooling for CPV dense array receivers, AIP Conf. Proc. 1881 (2017) 1–7, https://doi.org/10.1063/1.5001444.
[26] G. Laguna, et al., Dense array CPV receivers: impact of the cooling device on the net PV output for different illumination profiles, AIP Conf. Proc. 2012 (September) (2018), https://doi.org/10.1063/1.5053536.
[27] H. Azarkish, J. Barrau, P. Coudrain, G. Savelli, L.M. Collin, L.G. Frechette, Self-adaptive microvalve array for energy efficient fluidic cooling in microelectronic systems. Proceedings of the 16th InterSociety Conference on Thermal and Thermomechanical Phenomena in Electronic Systems, ITherm 2017, 2017, pp. 522–529, https://doi.org/10.1109/ITHERM.2017.7992531.
[28] G. Laguna, et al., Microfluidic cell cooling system for electronics, THERMINIC 2017 - 23rd International Workshop on Thermal Investigations of ICs and Systems 2017-Janua (September) (2017) 1–4, https://doi.org/10.1109/THERMINIC.2017.8233790.
[29] D.C. Dickson, Photo-voltaic Semiconductor Apparatus or the like, 1960, pp. 1956–1958.
[30] R. Norman, et al., On-sun testing of a 100-shingled-cell dense receiver array at ~50 W/cm2 using overlapped single-axis foci, AIP Conf. Proc. 2012 (2018), https://doi.org/10.1063/1.5053497.
[31] Spectrolab-Inc, CPV Point Focus Solar Cells, Data sheet, 2011, pp. 11–12.
[32] M. McCarthy, N. Tiliakos, V. Modi, L.G. Fréchette, Temperature-regulated nonlinear microvalves for self-adaptive MEMS cooling, J. Microelectromech. Syst. 17 (4) (2008) 998–1009, https://doi.org/10.1109/JMEMS.2008.927742.
[33] MathWorks, List of pre-parameterized components Simscape electrical [Online]. Available: https://es.mathworks.com/help/sps/ug/pre-parameterized-components.html#responsive_offcanvas. (Accessed 23 October 2024).
[34] OmniOn Power, "Data Sheet for non-isolated DC-DC power modules, Naos Raptor 40A." Accessed: Oct. 31, 2024. [Online]. Available: https://www.mouser.ec/datasheet/2/167/NSR040A0X_DS-1920160.pdf.
[35] Á. Fernández, et al., Assessment of the impact of non-uniform illumination and temperature profiles on a dense array CPV receiver performance, Sol. Energy 171 (Sep. 2018) 863–870, https://doi.org/10.1016/j.solener.2018.07.001.
[36] G. Laguna, et al., Microfluidic cell cooling system for electronics, THERMINIC 2017 - 23rd International Workshop on Thermal Investigations of ICs and Systems 2017-Janua (September) (2017) 1–4, https://doi.org/10.1109/THERMINIC.2017.8233790.
[37] M.L. Katche, A.B. Makokha, S.O. Zachary, M.S. Adaramola, A Comprehensive Review of Maximum Power Point Tracking (MPPT) Techniques Used in Solar PV Systems, MDPI, Mar. 01, 2023, https://doi.org/10.3390/en16052206.
[38] Z.M.S. Elbarbary, M.A. Alranini, Review of maximum power point tracking algorithms of PV system, Front. Eng. Built Environ. 1 (1) (Jul. 2021) 68–80, https://doi.org/10.1108/febe-03-2021-0019.